photonics

MDPI

Article

Quasi-BIC Terahertz Metasurface-Microfluidic Sensor for Organic Compound Detection

Liang Wang, Kang Chen, Jiahao Niu, Bo Zhang *, Qi Lu, Wei Yu, Yanan Xiao, Yi Ni and Chengkun Dong *

Engineering Research Center of IoT Technology Applications (Ministry of Education), School of Integrated Circuits, Jiangnan University, Wuxi 214122, China

* Correspondence: zhangb2018@jiangnan.edu.cn (B.Z.); dongchengkun@jiangnan.edu.cn (C.D.)

Abstract

Bound states in the continuum (BICs) can be transformed into quasi-bound states (quasi-BICs) via intentional symmetry breaking, thereby enabling ultrahigh-*Q* resonances critical for refractometric sensing applications. To advance detection capabilities for organic analytes, we proposed an all-dielectric metasurface monolithically integrated within a microfluidic channel. Mirror symmetry was intentionally disrupted through a cylindrical perturbation applied to one of two identical elliptical resonators, which excited a quasi-BIC mode at 1.9591 THz with a numerically validated *Q*-factor of 1959. This resonance manifested an absorption peak approaching unity, featuring a full-width at half-maximum (FWHM) of merely 1 GHz. Multipolar decomposition revealed that the mode originated from a synergistic electric-quadrupole (EQ)–magnetic-dipole (MD) pair, wherein the EQ contribution exceeded the MD counterpart by 20%. Capitalizing on this high-*Q* resonance, the sensor attained a sensitivity of 240 GHz per refractive-index unit (GHz RIU^{-1}) and a figure of merit (FOM = S/FWHM) of 240, while demonstrating robust performance against fabrication tolerances spanning −4% to +4%. Additionally, we verified that oblique-incidence illumination could activate a quasi-BIC within the identical spectral band, circumventing the need for structural asymmetry and thus expanding operational versatility. Benefiting from its geometric simplicity and competitive performance, this architecture exhibited substantial potential for on-chip sensing of organic compounds.

Keywords: terahertz sensor; metasurface; BICs; quasi-BICs; *Q*-factor; microfluidic

1. Introduction

Optical sensors are pivotal in modern detection systems, prized for their non-destructive nature and high sensitivity [1,2]. Their performance is fundamentally governed by the strength of light–matter interaction, which can be significantly enhanced by trapping light in resonant structures. BICs offer an ideal mechanism for this purpose. Initially proposed in quantum mechanics [3], BICs describe waves that remain perfectly confined even though their energy lies within the spectrum of radiating waves. In photonics, they give rise to resonances with a theoretically infinite *Q*-factor and near-zero linewidth, making them highly attractive for sensing applications [4–6]. Traditional BICs are typically protected by structural symmetry; however, by breaking this symmetry intentionally, they can be transformed into quasi-BICs, which retain ultrahigh *Q*-factors while becoming spectrally observable [7–10]. Ultra-narrow linewidths and correspondingly high *Q*-factors are essential for high-resolution refractive-index sensing [11]. By harnessing the sharp

Check for updates

Received: 26 December 2025
Revised: 19 January 2026
Accepted: 28 January 2026
Published: 29 January 2026

Copyright: © 2026 by the authors. Licensee MDPI, Basel, Switzerland. This article is an open access article distributed under the terms and conditions of the Creative Commons Attribution (CC BY) license.

absorption peaks of quasi-BICs, such resonances enable the detection of minute refractive-index variations, offering a promising route toward label-free, highly sensitive photonic sensors [12–17].

To harness such high-Q resonances for practical sensing, microfluidic technology provides an ideal platform. By integrating a metasurface absorber with a microchannel whose height is tuned to the micrometer scale, the device forms a Fabry–Pérot cavity that confines incident terahertz energy precisely within the analyte region; the solution effectively acts as the cavity dielectric, overlapping with the zone of maximum local field enhancement and thereby boosting sensitivity without increasing sample volume [18–21]. Furthermore, confining the liquid to a thickness of a few micrometers significantly suppresses the strong terahertz absorption by water [20,22], while still allowing molecular-specific interaction with the enhanced near-field of the quasi-BIC. This synergy—ultra-sharp resonances for spectral resolution, strong local fields for signal amplification, and microfluidic delivery for minimized water background—establishes a promising platform for label-free, trace-level detection of organic compounds in aqueous environments [23–26].

The state-of-the-art in terahertz metasurface sensing has witnessed considerable progress in recent years. As one example, Yang et al. reported a 3D double-I-shaped metasurface integrated with microfluidics that achieved 832 GHz RIU^{-1} sensitivity, yet suffered from a modest FOM of ~41.6 imposed by its 20 GHz linewidth, while its 1.44 THz operating frequency missed the higher-frequency molecular-fingerprint region entirely [22]. In parallel, Li et al. employed a quasi-BIC double-split-ring array attaining a Q-factor > 175 and 598 GHz RIU^{-1} sensitivity; however, the absence of on-chip fluidics confined its application to gas-phase or bulk dielectric detection exclusively [27]. Li and co-authors also demonstrated a symmetric, E-shaped, four-band metasurface providing 200 GHz RIU^{-1} sensitivity at Q-factor $\approx$ 177, though its FOM was merely 26.7, and the lack of integrated microfluidics precluded direct liquid-phase analysis [28]. Fu et al. described a four-strip graphene-based sensor operating at 2.58 THz and 6.07 THz, attaining 1.627 THz RIU^{-1} sensitivity; nonetheless, it exhibited a low Q-factor of 29.6, a modest FOM of just 3.9, and critically lacked microfluidic demonstration [29]. Collectively, prior methodologies—frequently constrained by sub-45 FOMs, absent integrated microfluidics, or functionality removed from the molecule-rich >1.5 THz regime—remain fundamentally incapable of simultaneously merging high sensitivity, elevated FOM, and seamless liquid compatibility into a single, unified, fabrication-friendly architecture.

In this work, we introduce a microfluidic-embedded, all-dielectric metasurface that broke symmetry to realize quasi-BIC behavior, functioning within the 1.9–2.0 THz spectral window. The microfluidic design, optimized at a channel height of 48 μm, positioned the analyte within the cavity directly, thereby enabling the liquid to serve as the functional dielectric of the absorber. This monolithic integration concurrently yielded a refractive-index sensitivity of 240 GHz RIU^{-1} and a FOM surpassing 200, thereby confirming that employing the channel medium as the active dielectric substantially enhanced sensing capabilities. By applying a cylindrical perturbation to one of a pair of identical elliptical blocks, we disrupted mirror symmetry and evoked a quasi-BIC exhibiting a measured Q-factor of 1.9×10^3. Analysis via multipolar decomposition indicated the resonance originated from a synergistic electric quadrupole (EQ)–magnetic dipole (MD) pair, wherein the EQ contribution surpassed the MD counterpart by 20%, resulting in tight confinement of the enhanced electromagnetic field within the channel volume. Capitalizing on this ultra-sharp resonance, the sensor realized a competitive FOM of 240 while preserving stable sensing performance across fabrication tolerances of $\pm$4%, placing it favorably among comparable metasurface platforms. Additionally, we demonstrate that oblique-incidence excitation could activate the identical quasi-BIC mode, eliminating the necessity for structural asym-

metry and affording an extra dimension for dynamic tuning. These findings validated a straightforward, high-performance pathway toward integrated refractometric sensing of organic analytes and furnished an extensible foundation for terahertz spectroscopy on lab-on-a-chip platforms.

2. Structure Design and Numerical Model

Figure 1a shows the 3D schematic of the proposed microfluidic sensor. The structure consists of a vertically stacked sequence: a quartz capping layer, a silicon metasurface slab, a microfluidic channel, a gold reflector, and a silicon substrate. A cross-sectional view in the x–z plane (Figure 1b) illustrates the layer thicknesses: h1 = 50 μm (quartz), h2 = 48 μm (channel), h3 = 200 μm (substrate), t1 = 30 μm (metasurface), and 200 nm for the gold mirror (exceeding the skin depth of gold at the operating frequencies to ensure total reflection) [20]. The unit cell, depicted in Figure 1c, has periods of Px = 98 μm and Py = 80 μm. It contains two identical elliptical silicon blocks (major axis b = 22 μm, minor axis a = 19 μm) centered at x = Px/4 and x = 3 Px/4, with the lattice assumed to be infinite in the x and y directions. To break the structural symmetry, a cylindrical silicon post (radius r = 18 μm, height t2) was placed atop one of the ellipses; the asymmetry degree was thus controlled by the parameter t2. All simulations were performed using the Wave Optics module in COMSOL Multiphysics 6.2. Silicon (both substrate and metasurface) was modeled as a dispersionless dielectric with a permittivity of $\varepsilon = 11.7$, while the quartz superstrate was assigned $\varepsilon = 3.9$. A plane wave with the electric field polarized along the y-direction and propagating normally toward the sensor stack (wave vector $k \parallel -z$) was employed as the excitation source.

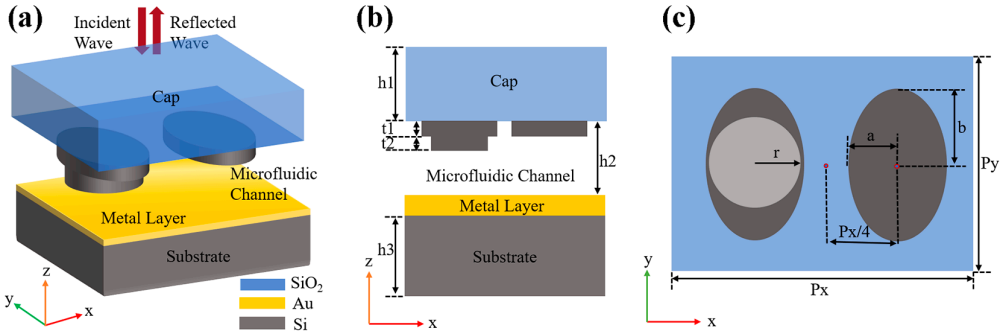


Figure 1. Microfluidic sensor integrated with a quasi-BIC metasurface: (**a**) Three-dimensional schematic of the device. (**b**) Cross-sectional view highlighting the thicknesses of the cap, channel, and metasurface layers. (**c**) Top view of the unit cell, illustrating the detailed geometric parameters of the meta-atom: minor axis a, major axis b, cylinder radius r, and lattice periods Px and Py.

3. Results and Discussion

In the perfectly symmetric structure (with the perturbation height t2 = 0), the symmetry-protected BIC remained decoupled from free-space radiation, resulting in a theoretically infinite *Q*-factor and no observable resonance in the absorption spectrum. Introducing a structural asymmetry by setting t2 = 3 μm broke the geometric mirror symmetry, converted the non-radiative BIC into a leaky quasi-BIC, and reduced the *Q*-factor to a finite, measurable value. Figure 2 compares these two regimes: while no resonance appeared under the ideal BIC condition, the quasi-BIC exhibited a near-unity absorption peak (≈1) within the same spectral window when the microfluidic channel was filled with a medium of refractive index $n = 1.3$, confirming the efficient excitation of the formerly dark mode under a realistic sensing condition.

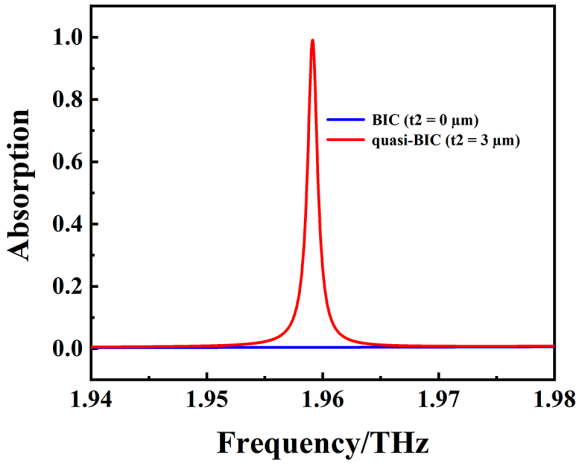


Figure 2. Simulated absorption spectra of a quasi-BIC compared to a BIC. The red curve represents the quasi-BIC model, exhibiting a pronounced absorption peak with a high *Q*-factor, while the blue curve corresponds to the BIC model, showing no absorption due to its perfect confinement without radiation loss.

Figure 3a shows the absorption spectra of the microfluidic sensor for increasing symmetry-breaking heights t2 = 0, 0.5, 1, 1.5, and 2 μm. When t2 = 0 μm (perfectly symmetric meta-atom), the bound state in the continuum remained dark and no resonance was observed. For any t2 > 0, mirror symmetry was broken, the mode became radiative, and a distinct absorption peak emerged with an amplitude that grew as t2 increased. The two-dimensional map in Figure 3b summarizes this evolution, where color represents absorbance while t2 was swept from 0 to 2 μm. As t2 decreased continuously, the resonance linewidth narrowed monotonically, its center frequency blue-shifted, and the *Q*-factor rose, consistently approaching the ideal BIC limit.

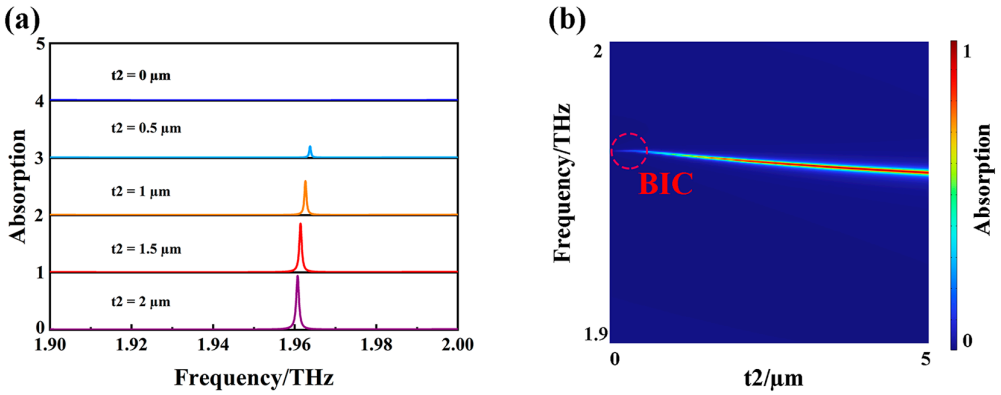


Figure 3. (**a**) Simulated absorption spectra for varying values of the structural asymmetry parameter t2, illustrating the transition from a BIC to a quasi-BIC with increasing t2. (**b**) Two-dimensional map showing the dependence of the resonance frequency on both the asymmetry parameter t2 and frequency, highlighting the BIC point where no absorption occurs.

Figure 4 quantifies the correlation between structural asymmetry and resonance characteristics. Starting from the ideal limit of t2 $\rightarrow$ 0 (perfect symmetry), the mode converges to a true symmetry-protected BIC with a theoretically diverging *Q*-factor. As t2 was increased infinitesimally from zero to a non-zero but still extremely small value, a quasi-BIC emerged with a dramatically high *Q*-factor on the order of $\approx$4000, illustrating the rapid *Q*-degradation that accompanies even minimal symmetry breaking. With further increase in t2, the *Q*-factor decayed monotonically due to enhanced radiative leakage, wherein a larger geometric perturbation coupled the confined mode more strongly to free-space

radiation, broadening the resonance linewidth and reducing the *Q*-factor. Concurrently, the FWHM broadened correspondingly from this ultra-narrow state. For a practical device design, setting t2 = 3 μm produced a readily measurable quasi-BIC state with a *Q*-factor of ~1900, which was adopted as the operating point in the following sensing performance analysis. Beyond theoretical analysis, the proposed architecture demonstrates experimental feasibility through mature CMOS fabrication processes. Specifically, the sensor capping layer can be fabricated via a straightforward sequence: (1) PECVD deposition of SiO_2 on a silicon substrate; (2) microscale patterning by standard UV photolithography with spin-coated photoresist; (3) wafer bonding to quartz using optical adhesive; and (4) selective removal of SiO_2 by CHF_3/CF_4 plasma etching, finalized by DRIE [30]. This process flow underscores the practical viability of our design.

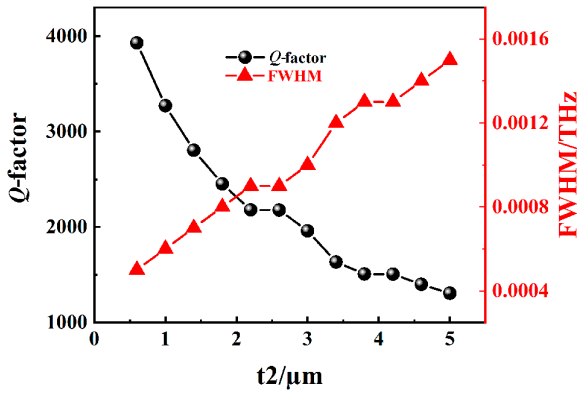


Figure 4. Dependence of the *Q*-factor on the structural-asymmetry parameter t2. As t2 increases from near-zero to 5 μm, *Q*-factor decreases monotonically, signaling the transition from a BIC to a quasi-BIC with progressively stronger energy leakage.

Figure 5 systematically evaluates the influence of individual geometric parameters on the spectral response of the perturbed sensor (with t2 fixed at 3 μm). As the lattice period Px increased from 94 μm to 102 μm in steps of 2 μm (Figure 5a), the quasi-BIC resonance red-shifted monotonically. The peak absorbance showed only minor variation, while the FWHM remained nearly constant, leaving the *Q*-factor essentially unchanged. A corresponding scan of Py from 76 μm to 84 μm (Figure 5b, same step size) resulted in a negligible frequency shift and only a slight change in absorption depth. By contrast, dimensions within the unit cell exerted a stronger influence on the resonance frequency. Increasing the cylinder radius a from 19 μm to 23 μm (1 μm step, Figure 5c) produced a red shift larger than that induced by comparable changes in Px or Py, yet the linewidth and *Q*-factor were preserved within the numerical uncertainty. The most sensitive parameter was the lateral split distance b: a 1 μm increase from 20 μm to 24 μm (Figure 5d) yielded the largest spectral displacement, again without measurable broadening or degradation in *Q*-factor. Because each geometric degree of freedom produced a distinct and predictable frequency offset, selective adjustment of the lattice periods or meta-atom dimensions enabled the absorption peak to be positioned at will, offering a versatile design knob for application-specific sensors.

The distinct spectral response of our quasi-BIC metasurface to geometric perturbations (Figure 5) necessitates a mechanistic explanation at the fundamental multipolar level. To this end, we employed a Cartesian multipole decomposition [28,29] of the induced current density *J(r)*. This framework rigorously partitions the total scattering response of the meta-atom into orthogonal contributions from electric dipole (ED), magnetic dipole (MD), electric quadrupole (EQ), magnetic quadrupole (MQ), and toroidal dipole (TD)

components. Projecting the simulated *J(r)* onto this basis yielded the complex amplitude of each multipole, whose relative radiative strength was then quantified.

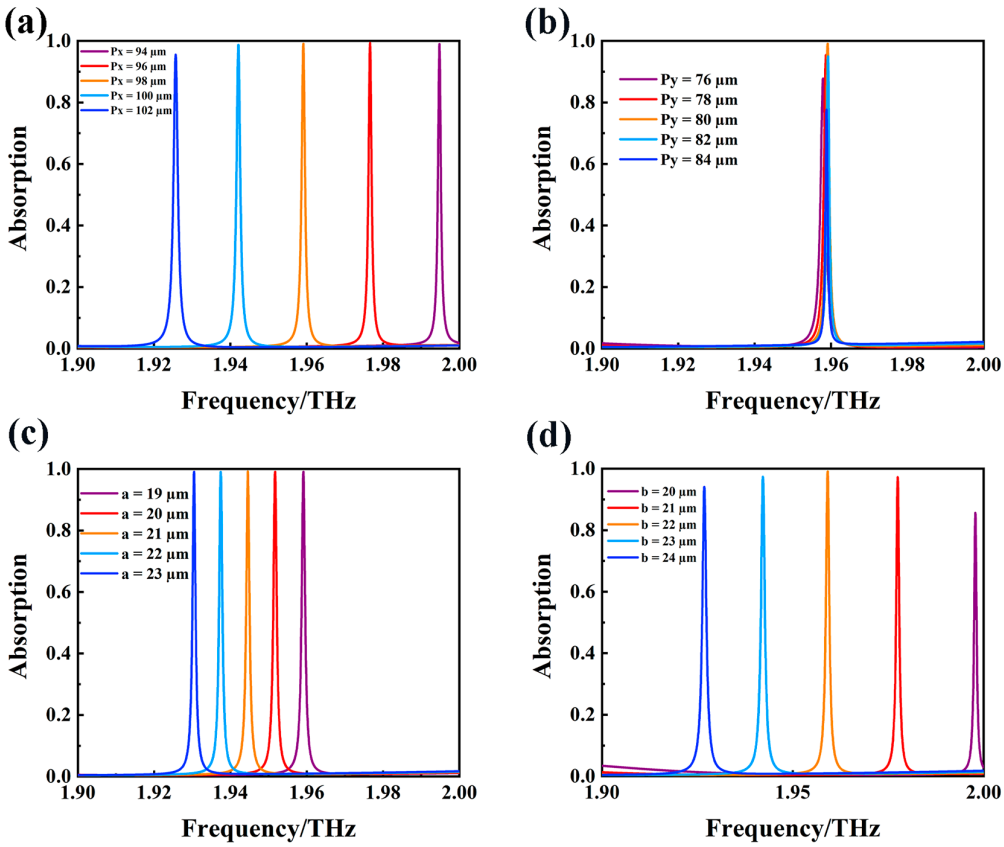


Figure 5. Simulated absorption spectra illustrating the influence of structural parameters on the quasi-BIC resonance: (**a**) Lattice period Px (94–102 μm); increasing Px induces a red-shift. (**b**) Lattice period Py (76–84 μm); negligible frequency shift is observed. (**c**) Minor axis a of the elliptical blocks (19–23 μm); larger a causes a red-shift. (**d**) Major axis b (20–24 μm); increasing b produces a red-shift. In all cases, the peak amplitude and linewidth remain essentially unchanged, underscoring the flexible tunability of the metasurface sensor.

For our specific design, the dominant interactions were captured by terms up to the quadrupolar order. The corresponding multipole moments—the electric dipole ED_α, magnetic dipole MD_α, toroidal dipole TD_α, electric quadrupole $EQ_{\alpha\beta}$, and magnetic quadrupole $MQ_{\alpha\beta}$—were computed via volume integration of *J(r)* over the unit cell using the following expressions [31,32]:

$$ED_\alpha = \frac{1}{i\omega}\int d^3 r J_\alpha \quad (1)$$

$$MD_\alpha = \frac{1}{2c}\int d^3 r [r \times J]_\alpha \quad (2)$$

$$TD_\alpha = \frac{1}{10c}\int d^3 r \left[(r \times J) r_\alpha - 2r^2 J_\alpha\right] \quad (3)$$

$$EQ_{\alpha\beta} = \frac{1}{2i\omega}\int d^3 r \left[r_\alpha J_\beta + r_\beta J_\alpha - \frac{2}{3}(r \times J)\delta_{\alpha\beta}\right] \quad (4)$$

$$MQ_{\alpha\beta} = \frac{1}{3c}\int d^3 r \left[r_\beta (r \times J)_\alpha - (r \times J)_\beta r_\alpha\right] \quad (5)$$

Here, ω is the angular frequency, c the speed of light, and $\delta_{\alpha\beta}$ the Kronecker delta. The scattered power radiated by each multipole channel is:

$$I_{ED} = \frac{2\omega^4}{3c^3} | ED |^2 \quad (6)$$

$$I_{MD} = \frac{2\omega^4}{3c^3} | MD |^2 \quad (7)$$

$$I_{TD} = \frac{2\omega^6}{3c^5} | TD |^2 \quad (8)$$

$$I_{EQ} = \frac{\omega^6}{5c^5} | EQ_{\alpha\beta} |^2 \quad (9)$$

$$I_{MQ} = \frac{\omega^6}{40c^5} | MQ_{\alpha\beta} |^2 \quad (10)$$

By evaluating these moments at the resonance frequency, we identified which multipole channels drove the high-Q quasi-BIC. Crucially, this analysis allowed us to trace how the dominant contributions (e.g., the ED, MD, or EQ) evolved with structural detuning, thereby linking the macroscopic spectral shifts in Figure 5 directly to microscopic changes in the underlying current topology within the silicon meta-atom.

Multipolar decomposition of the quasi-BIC mode at t2 = 3 μm identified a hybrid electric quadrupole–magnetic dipole (EQ-MD) pair as the dominant scattering source. The far-field radiation spectra in Figure 6a confirmed that the EQ and MD contributions surpassed all other Cartesian multipoles, with the EQ amplitude being consistently about 1.2 times larger than that of the MD. Furthermore, decomposition of the MD scattering power along the x, y, and z directions (Figure 6b) revealed that the z-component exhibited the largest magnitude, indicating that the z-oriented MD mode provided the predominant contribution to the quasi-BIC resonance.

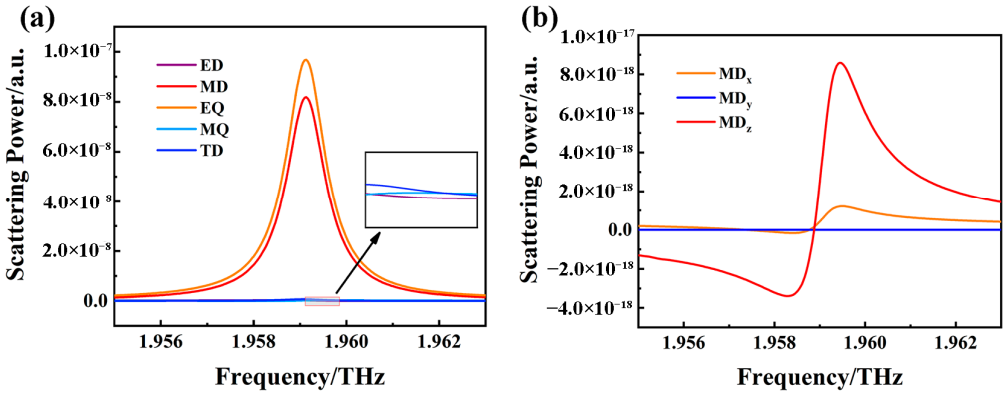


Figure 6. Multipolar decomposition analysis of the quasi-BIC resonance at 1.9591 THz. (**a**) Total scattering power spectra showing the contributions from ED, MD, EQ, MQ, and TD, with MD and EQ being the dominant terms. (**b**) Decomposition of the MD scattering power into its x, y, and z components, highlighting the significant contribution of the z-component to the quasi-BIC resonance. The sharp peaks at 1.9591 THz are primarily due to the EQ and MD terms, with negligible contributions from MQ, TD, and ED.

The instantaneous electric-field distribution in the x–y plane (Figure 7a, red arrows) reveals two counter-rotating displacement-current loops, a hallmark of a magnetic-dipole (MD) mode confined within the unit cell. The corresponding z-component of the magnetic field (Figure 7c) exhibits two anti-parallel flux bundles, confirming that paired MD moments with opposite polarity undergo imperfect far-field cancelation, yielding a resid-

ual MD contribution that remains subordinate to the electric-quadrupole (EQ) channel. Figure 7d, where arrows indicate magnetic-field orientation in the x–y cross-section, further substantiates this incomplete cancellation: the right-side magnetic flux substantially exceeds its left-side counterpart. Combined with the opposite polarity of the dual vortices shown in Figure 7c, this asymmetry accounts for the finite net MD signature. In contrast, the z-component of the electric field in the x–y plane (Figure 7b) displays two anti-aligned electric-dipole pairs, a configuration that directly projects onto the EQ tensor. Consequently, the high-*Q* absorption peak arises from the synergistic interplay between a strongly excited EQ and a partially canceled MD, with the EQ providing the dominant scattering pathway.

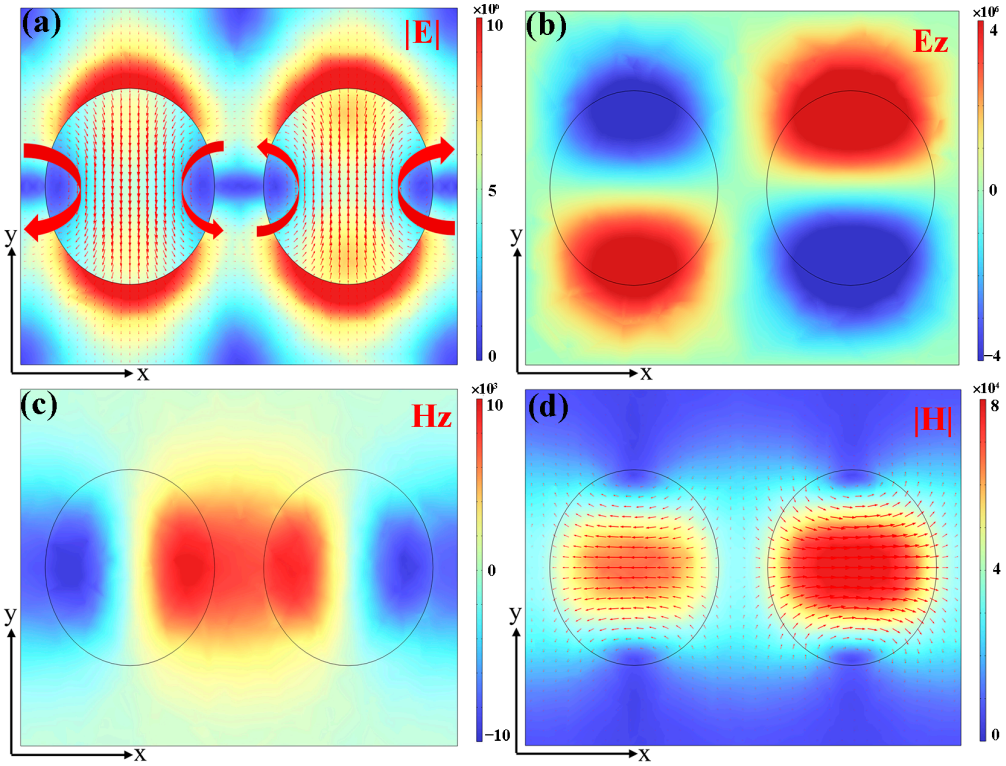


Figure 7. Simulated field distributions of the quasi-BIC mode (ellipse denotes the metasurface resonant structure boundary). (**a**) The electric-field magnitude (|E|) in the x–y plane, 10 μm above the channel, with red arrows indicating the displacement-current vortices. (**b**) The Ez component of the electric field in the x–y plane, showing two opposing electric-dipole pairs. (**c**) The Hz component of the magnetic field across the x–y plane within the channel, exhibiting anti-parallel magnetic-flux bundles. (**d**) The x–y cross-sectional view of the magnetic field, with red arrows depicting the magnetic-field lines. The color intensity corresponds to the field magnitude, with red representing high magnitude and blue representing low magnitude.

As a microfluidic sensor, its resonance frequency was determined by the overlap between the optical mode and the analyte-filled volume. Figure 8 illustrates the influence of the channel height h2 on the quasi-BIC signature. When h2 was increased from 42 μm to 54 μm (Figure 8a), the absorption peak red-shifted continuously: the silicon metasurface occupied a smaller fraction of the channel, lowering the volume-averaged refractive index because the analyte's index was much lower than that of silicon ($n_{\text{analyte}} \ll n_{\text{Si}}$). Simultaneously, the absorbance decreased once h2 deviated from the optimal value of 48 μm; this degradation was more pronounced for shallower channels. At heights below 48 μm, the upper and lower quartz walls confined the EQ displacement current loops (Figure 7a) and truncated the MD vortices (Figure 7d). The resulting incomplete multipole rotation

weakened both the EQ and the residual MD contributions, so the cooperative EQ-MD efficiency was maximized only at h2 = 48 μm—hence our selection of this height.

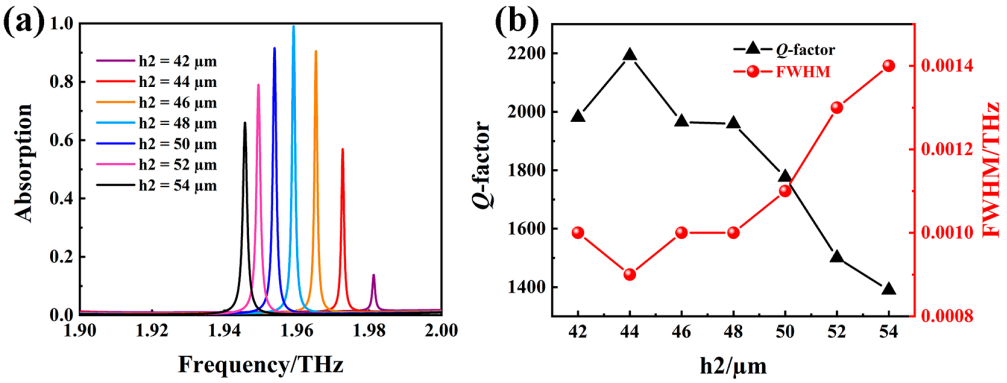


Figure 8. (**a**) Simulated absorption spectra illustrating the impact of varying the channel height h2 on the quasi-BIC resonance peak. (**b**) The variation in the *Q*-factor and FWHM as a function of the channel height h2, indicating the trend that can be utilized to optimize these parameters.

Figure 8b summarizes the evolution of the resonance linewidth. As h2 increased, radiative leakage into the extended low-index fluid region rose, which broadened the FWHM and reduced the *Q*-factor from about 2000 (h2 = 42 μm) to 1400 (h2 = 54 μm). At the optimal height of 48 μm, the device maintained a balanced compromise: *Q*-factor = 1959 and FWHM = 0.001 THz, offering both a narrow linewidth and strong absorption for on-chip spectroscopic sensing.

Owing to its high-*Q* quasi-BIC, the proposed microfluidic platform was well-suited for refractive-index (RI) sensing. We evaluated its sensing performance using two standard metrics: the sensitivity S = $\Delta f / \Delta n$ and the figure of merit FOM = S/FWHM [33–36]. Figure 9a shows the absorption spectra as the analyte RI was increased from 1.30 to 1.40 in steps of 0.02. The quasi-BIC peak shifted uniformly toward lower frequencies without measurable broadening or amplitude loss. A linear fit to the resonance shift (Figure 9b) yielded a sensitivity S = 240 GHz RIU^{-1}. With an average FWHM of 1 GHz, this corresponds to a FOM of 240, which ranks among the high values reported for silicon-based terahertz metasurface sensors and establishes a significant improvement over many current designs. The RI interval examined here covered a wide variety of organic solvents (e.g., methanol, diethyl ether) [37,38], which demonstrated the device's potential for label-free detection of small-molecule analytes and on-chip chemical monitoring.

The impact of material losses on sensing performance was subsequently investigated. Loss tangents of 0.001, 0.0004, and 0.00002 were assigned to the analyte, quartz, and silicon, respectively. Figure 10 illustrates the sensing characteristics under realistic lossy conditions. Notably, Figure 10a demonstrates that while the FWHM of the absorption peak broadens and the peak absorptance declines relative to the lossless scenario, the resonance frequencies for various refractive indices remain unchanged. This confirms that the refractive-index sensitivity is retained at 240 GHz RIU^{-1}. Furthermore, Figure 10b reveals that the sensor's FOM sustains values between 130 and 140, thereby preserving robust performance. Importantly, a monotonic variation in absorption intensity with refractive index is observed, opening up opportunities for absorbance-based sensing. Collectively, these results demonstrate that the sensor maintains high-performance sensing capabilities even when material losses are considered.

During device fabrication, inevitable processing tolerances may degrade sensor performance. To assess stability, we systematically varied the manufacturing error of parameter t2 and evaluated the resulting changes in functionality. Figure 11 presents the simula-

tion results obtained with the analyte refractive index set to 1.3. Figure 11a reveals that tolerances within ±4% neither shifted the resonance frequency nor altered the peak absorbance. Figure 11b further shows the sensitivity and FOM when the analyte index was changed from 1.3 to 1.32; under the same tolerance range, the sensitivity varied between 235 and 240 GHz RIU^{-1}, while the FOM remained essentially constant at approximately 238. These findings demonstrate that the sensor maintained excellent performance even in the presence of realistic fabrication deviations.

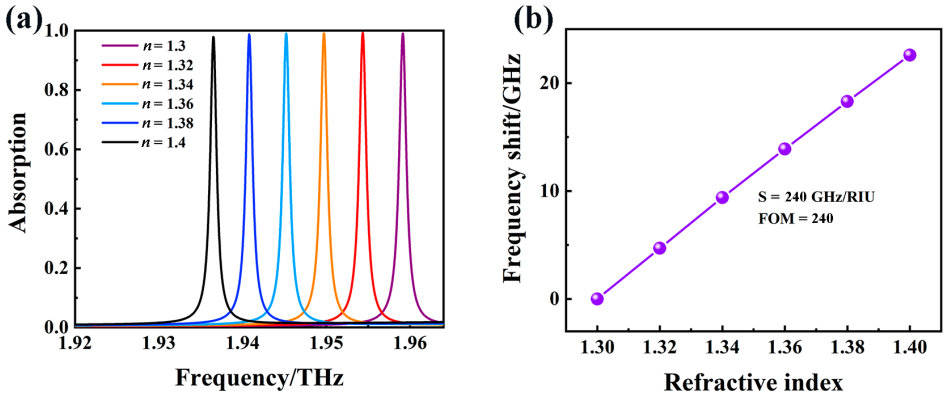


Figure 9. (**a**) Simulated absorption spectra for different refractive indices (n) ranging from 1.30 to 1.40, demonstrating the sensor's ability to resolve small refractive index changes. (**b**) Frequency shift as a function of refractive index, highlighting the sensor's sensitivity (S = 240 GHz RIU^{-1}) and FOM = 240.

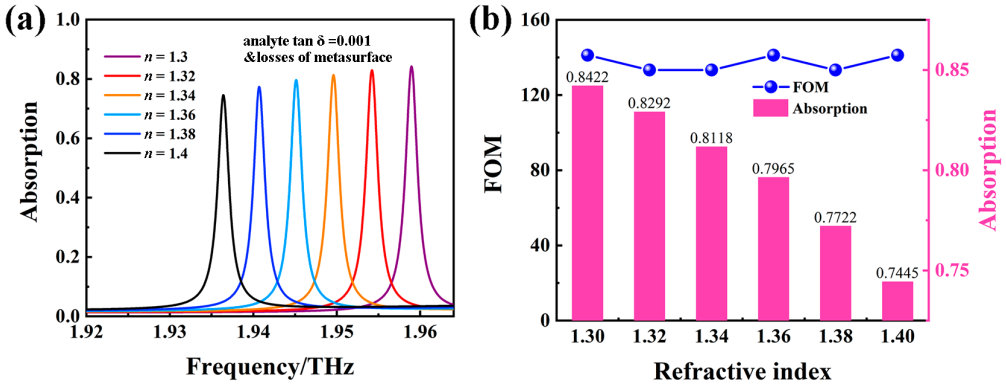


Figure 10. Sensor performance with material losses included: (**a**) Absorption spectra for refractive indices from 1.30 to 1.40, showing broadened peaks and reduced peak absorptance but constant resonance frequencies, preserving a sensitivity of 240 GHz RIU^{-1}. (**b**) FOM remains high (130–140) with decreasing absorption, indicating robust sensing performance despite losses.

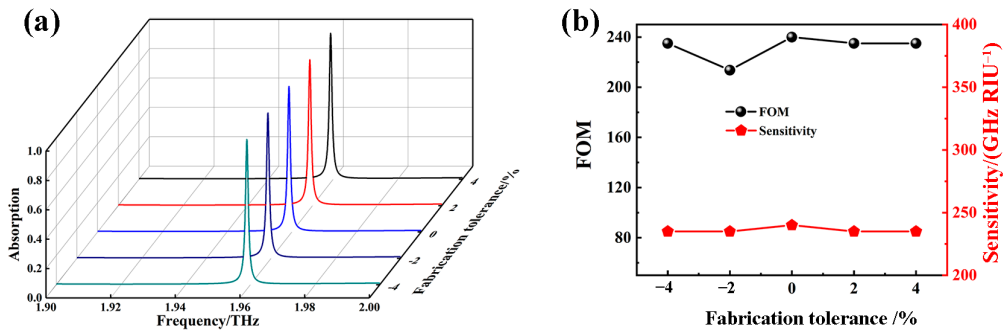


Figure 11. (**a**) Simulated absorption spectra demonstrating the impact of fabrication tolerances on the sensor's performance. (**b**) Plot of the FOM and sensitivity as a function of fabrication tolerance.

As summarized in Table 1, which provides a curated comparison of selected recent (2020–2025) terahertz metasurface refractive-index sensors that report well-defined sensitivity and *Q*-factor, current devices in this field are frequently constrained either by the lack of integrated on-chip liquid handling or by a FOM that typically remains below 50. These limitations stem primarily from metallic ohmic losses or intrinsically low-*Q* resonances, which lead to broadened linewidths [39,40]. In contrast, our symmetry-broken, all-dielectric quasi-BIC design confines the optical field tightly within the 48 µm microchannel, resulting in a FWHM of about 1 GHz—significantly narrower than values reported in most prior studies included in this comparison. The FOM, defined as S/FWHM, inherently normalizes performance across different operational frequencies, thereby offering a fair and direct metric for comparing the overall sensing capability of various devices. The concurrent realization of a high FOM (>200) together with monolithic microfluidic integration has rarely been achieved in the sensor platforms surveyed, underscoring the distinct advantage of our design for trace-level detection of organic analytes.

In addition to structural symmetry breaking, we examined an alternative route to numerically excite the quasi-BIC by varying the angle of incidence in simulation. Setting the asymmetry parameter t2 to zero, i.e., removing the cylindrical perturbation—restored full geometric symmetry in the model, yet a high-*Q* resonance could still be obtained by tilting the incident wave vector. Figure 12a illustrates the oblique incidence configuration, in which the incident angle θ was varied while the electric field remained polarized along the y direction. The resulting simulated absorption map (Figure 12b) showed a near-unity peak emerging between 1.9 and 2.0 THz; the resonance gradually broadened as θ increased from 0° to 5°, exhibiting the characteristic evolution from a symmetry-protected BIC to a radiative quasi-BIC. This angle-driven excitation enriched the sensor's operational modalities by providing a reconfigurable, structure-free tuning knob that could be implemented in real time without any fabrication overhead.

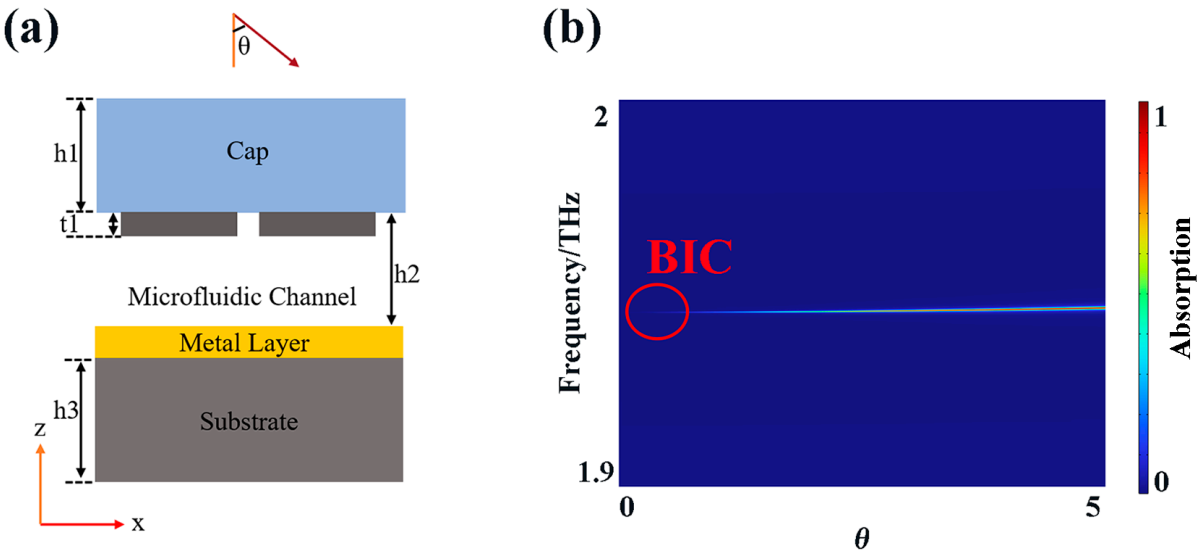


Figure 12. (**a**) Schematic of the sensor structure showing the cap, microfluidic channel, metal layer, and substrate with respective thicknesses h1, h2, and h3. The incident wave is depicted with an angle θ. (**b**) Frequency map as a function of angle θ, highlighting the BIC point where no absorption occurs, indicated by the red circle. The color scale represents the absorption intensity, with red being the highest and blue being the lowest.

Table 1. Comparative performance of simulated terahertz metasurface refractive-index sensors.

Refs.	Resonance Frequency/THz	Sensitivity/GHz RIU^{-1}	*Q*-Factor	FWHM/GHz	FOM	Liquid Compatibility
[41]	0.5	175	17.62	33	4.52	No
[42]	1.0976	142.76	/	28.5	5.01	No
[43]	0.5	0.54	57.4	/	50.7	No
[44]	0.9443	146.4	202.94	/	31.15	No
	0.6598	69.6	84.01	/	8.81	No
[45]	0.2	200	29.6	/	5.93	No
This work	1.9591	240	1959	1	240	Yes

4. Conclusions

We proposed and investigated a microfluidic integrated, all-dielectric metasurface sensor operating in the 1.9–2.0 THz band for label-free refractive index detection of organic liquids. The unit cell consists of two identical elliptical silicon blocks, with a cylindrical protrusion added to one of them to break mirror symmetry, thereby supporting a symmetry-protected BIC. This BIC was converted into a radiative quasi-BIC with a simulated ultra-high *Q*-factor of $\sim 1.9 \times 10^3$. Notably, a quasi-BIC absorption peak could also be efficiently generated within the same frequency band under a small oblique-incidence angle, even in a perfectly symmetric structure, providing an alternative excitation mechanism without structural modification. Multipolar decomposition showed that the resonance was dominated by an electric quadrupole moment, which tightly confined the enhanced field inside the 48 μm-high microchannel and thus strengthened the light–matter interaction. Our numerical results yielded a sensitivity of 240 GHz RIU^{-1} and an FOM of 240, both remaining insensitive to fabrication tolerances of ±4%. The resonance could be tuned by adjusting geometric parameters or the microchannel height without significant degradation in *Q*-factor. By breaking mirror symmetry to unite quasi-bound states with on-chip microfluidics, this work offers a practical and promising route toward terahertz spectroscopy of organic analytes. It is important to emphasize that all the results and performance metrics presented in this work, including the ultra-high *Q*-factor, sensitivity, and robustness analysis, are derived from comprehensive numerical simulations. These simulations serve as a critical and efficient proof-of-concept, allowing us to explore the design space, elucidate the underlying physical mechanisms (e.g., the EQ-MD dominant mode), and optimize the sensor parameters thoroughly before costly fabrication. The excellent performance predicted by our models establishes a strong theoretical foundation for this sensor architecture. Future work will focus on the experimental realization of the device, utilizing standard microfabrication and bonding techniques as outlined in the discussion, to validate these simulation results and demonstrate its practical sensing capabilities for real organic compounds.

Author Contributions: Conceptualization, B.Z., C.D., Y.X. and L.W.; methodology, L.W., K.C. and J.N.; software, Y.X., J.N. and L.W.; validation, B.Z., W.Y. and Q.L.; formal analysis, L.W. and Q.L.; investigation, B.Z., C.D. and Y.N.; resources, Y.X., Y.N. and C.D.; data curation, Y.N., W.Y. and K.C.; writing—original draft preparation, L.W. and B.Z.; writing—review and editing, B.Z., Q.L. and J.N.; visualization, B.Z., K.C. and L.W.; supervision, Y.N. and W.Y.; project administration, B.Z. and C.D.; funding acquisition, B.Z. and Q.L. All authors have read and agreed to the published version of the manuscript.

Funding: This work was supported by the Yangtze River Delta Innovation and Entrepreneurship Joint Carrier Demonstration Project (23002430100), the Wuxi Science and Technology Development Fund Project (K20241036), the National Natural Science Foundation of China (61903159), and the Natural Science Foundation of Jiangsu Province (BK20190617).

Data Availability Statement: The data that support the findings of this study are available from the first author or the corresponding authors upon reasonable request.

Conflicts of Interest: The authors declare no conflicts of interest.

References

1. Zhu, C.; Zhao, Z.X.; Shan, Z.J.; Yang, L.J.; Ji, S.J.; Yang, Z.H.; Zhang, Z.Y. Robust target detection of intelligent integrated optical camera and mmWave radar system. *Digit. Signal Process.* **2024**, *145*, 104336. [CrossRef]
2. Butt, M.A. Beyond the detection limit: A review of high-Q optical ring resonator sensors. *Mater. Today Phys.* **2025**, *58*, 101873. [CrossRef]
3. González, J.W.; Pacheco, M.; Rosales, L.; Orellana, P.A. Bound states in the continuum in graphene quantum dot structures. *Europhys. Lett.* **2010**, *91*, 66001. [CrossRef]
4. Yang, L.; Yu, S.L.; Li, H.; Zhao, T.G. Multiple fano resonances excitation on all-dielectric nanohole arrays metasurfaces. *Opt. Express* **2021**, *29*, 14905–14916. [CrossRef] [PubMed]
5. Krishna, A.S.L.; Menon, S.; Prosad, A.; Raghunathan, V. Mid-infrared quasi-BIC resonances with subwavelength slot mode profiles in germaniumbased coupled guided-mode resonance structures. *Photonics Res.* **2022**, *10*, 68–75. [CrossRef]
6. Chen, J.M.; Xue, C.Y.; Zheng, Y.Q.; Wu, L.Y.; Chen, C.; Han, Y. Micro-fiber-optic acoustic sensor based on high-Q resonance effect using Fabry-Perot etalon. *Opt. Express* **2021**, *29*, 16447–16454. [CrossRef]
7. Han, S.; Cong, L.Q.; Srivastava, Y.K.; Qiang, B.; Rybin, M.; Kumar, A.; Jain, R.; Lim, W.X.; Achanta, V.C.; Prabhu, S.S.; et al. All-Dielectric active terahertz photonics driven by bound states in the continuum. *Adv. Mater.* **2019**, *31*, 1901921. [CrossRef]
8. Zhong, H.K.; He, T.T.; Meng, Y.; Xiao, Q.R. Photonic bound states in the continuum in nanostructures. *Materials* **2023**, *16*, 7112. [CrossRef]
9. Zhong, H.K.; He, T.T.; Wang, Y.H.; Qi, T.C.; Meng, Y.; Li, D.; Yan, P.; Xiao, Q.R. Efficient polarization-insensitive quasi-BIC modulation by VO2 thin films. *Opt. Express* **2024**, *32*, 5862–5873. [CrossRef]
10. Lai, F.X.; Fan, Y.B.; Sha, X.B.; Deng, H.C.; Jiang, X.; Xiao, S.M.; Huang, C.; Song, Q.H. Ultrafast polarization modulation with high-purity chiral quasi-BIC metasurfaces. *Chin. Opt. Lett.* **2025**, *23*, 053605. [CrossRef]
11. Wang, B.X.; He, Y.H.; Lou, P.C.; Xing, W.H. Design of a dual-band terahertz metamaterial absorber using two identical square patches for sensing application. *Nanoscale Adv.* **2020**, *2*, 763–769. [CrossRef] [PubMed]
12. Chao, M.H.; Liu, Q.S.; Zhang, W.J.; Zhuang, L.Y.; Song, G.F. Mutual coupling of corner-localized quasi-BICs in high-order topological PhCs and sensing applications. *Opt. Express* **2022**, *30*, 29258–29270. [CrossRef] [PubMed]
13. Sun, J.X.; Hu, J.H.; Li, L.; Zhao, J.J. Robust high-Q quasi-BICs in double-layer high-contrast metagrating with temperature self-compensation for refractive index sensing. *J. Opt.* **2024**, *26*, 095801. [CrossRef]
14. Wang, Z.C.; Liang, T.X.; Zhang, H. Ultrahigh-Q quadrupole resonance quasi-BICs excited with different polarized light in an all-dielectric metasurface for refractive index sensing. *Opt. Commun.* **2025**, *591*, 132141. [CrossRef]
15. Zhao, Y.F.; Wu, Z.H.; Feng, Z.H.; Ning, T.Y. Ultra-sensitive refractive index sensing based on quasi-BICs in all-dielectric nanorod array. *Photonics* **2024**, *11*, 503. [CrossRef]
16. Jiao, R.Q.; Wang, Q.; Liu, J.J.; Shu, F.Z.; Pan, G.M.; Jing, X.F.; Hong, Z. High-Q quasi-bound states in the continuum in terahertz all-silicon metasurfaces. *Micromachines* **2023**, *14*, 1817. [CrossRef]
17. Maleki, J.; Fathi, D. Refractive index sensor based on fano-magnetic toroidal quadrupole resonance enabled by bound state in the continuum in all-dielectric metasurface. *Sci. Rep.* **2024**, *14*, 4110. [CrossRef]
18. Huang, S.T.; Hsu, S.F.; Tang, K.Y.; Yen, T.J.; Yao, D.J. Application of a terahertz system combined with an X-shaped metamaterial microfluidic cartridge. *Micromachines* **2020**, *11*, 74. [CrossRef]
19. Lan, F.; Luo, F.; Mazumder, P.; Yang, Z.Q.; Meng, L.; Bao, Z.Q.; Zhou, J.; Zhang, Y.X.; Liang, S.X.; Shi, Z.J.; et al. Dual-band refractometric terahertz biosensing with intense wave-matter-overlap microfluidic channel. *Biomed. Opt. Express* **2019**, *10*, 3789–3799. [CrossRef]
20. Hu, X.; Xu, G.Q.; Wen, L.; Wang, H.C.; Zhao, Y.C.; Zhang, Y.X.; Cumming, D.R.S.; Chen, Q. Metamaterial absorber integrated microfluidic terahertz sensors. *Laser Photon. Rev.* **2016**, *10*, 962–969. [CrossRef]
21. Liu, J.J.; Fan, L.L.; Shen, X.H. Terahertz microfluidic biosensor based on metamaterial absorber. *Optoelectron. Adv. Mater.-Rapid Commun.* **2023**, *17*, 1–7.
22. Yang, J.P.; Deng, H.; Xiong, Z.G.; Shang, L.P. Terahertz sensor based on a three-dimensional double I-type metamaterial integrated microfluidic channel. *Appl. Optics* **2021**, *60*, 3816–3822. [CrossRef] [PubMed]
23. Li, X.; Jiao, H.Y.; Zhu, M.Q.; Deng, T.; Sun, J.Y. A novel terahertz integrated sensor for liquid samples detections based on metamaterial and embedded microfluidic channels. *J. Phys. D-Appl. Phys.* **2023**, *56*, 025401. [CrossRef]
24. Liu, J.J.; Fan, L.L.; Wu, Y.P.; Chen, J.H.; Li, P. Research on high-sensitivity metamaterial-based terahertz microfluidic sensors for biological detection. *Optoelectron. Adv. Mater.-Rapid Commun.* **2025**, *19*, 328–336.

25. Sharma, S.; Singh, R.; Singh, P. Metamaterial-enhanced terahertz slot high Q-factor antenna for wideband microfluidic sensing of water permittivity characterization. *J. Nanophotonics* **2025**, *19*, 036004. [CrossRef]
26. Xin, W.; Wang, J. Terahertz metamaterial absorber sensor based on three-dimensional split-ring resonator array and microfluidic channel. *Acta Opt. Sin.* **2020**, *40*, 1904001.
27. Li, S.T.; Wang, Q.; Chen, C.; Liu, Z.Y.; Ren, G.H.; Ren, Z.; Wang, R.X. High-Q factor terahertz metamaterial sensor based on quasi-BIC. *Opt. Mater. Express* **2024**, *14*, 1509–1519. [CrossRef]
28. Li, L.; Ge, H.Y.; Jiang, Y.Y.; Li, G.M.; Wang, F.; Lv, M.; Ji, X.D.; Jia, Z.Y.; Li, Z.; Zhang, Y. A four-band terahertz metamaterial sensor based on symmetric E-shaped structure. *Coatings* **2022**, *12*, 1694. [CrossRef]
29. Fu, M.X.; Ye, Y.C.; Niu, Y.Y.; Guo, S.S.; Wang, Z.Y.; Liu, X.Y. Graphene-based tunable dual-frequency terahertz sensor. *Nanomaterials* **2024**, *14*, 378. [CrossRef]
30. Zograf, G.; Koshelev, K.; Zalogina, A.; Korolev, V.; Hollinger, R.; Choi, D.Y.; Zuerch, M.; Spielmann, C.; Luther-Davies, B.; Kartashov, D.; et al. High-harmonic generation from resonant dielectric metasurfaces empowered by bound states in the continuum. *ACS Photonics* **2022**, *9*, 567–574. [CrossRef]
31. Yu, S.L.; Wang, Y.S.; Gao, Z.A.; Li, H.; Song, S.Z.; Yu, J.G.; Zhao, T.G. Dual band polarization insensitive toroidal dipole quasi-bound states in the continuum in a permittivity-asymmetric all-dielectric meta-surface. *Opt. Express* **2022**, *30*, 4084–4095. [CrossRef] [PubMed]
32. Guo, L.C.; Gao, Y.C. High-Q resonances induced by toroidal dipole bound states in the continuum in terahertz metasurfaces. *Crystals* **2025**, *15*, 96. [CrossRef]
33. Romain, X.; Baida, F.; Boyer, P. Extended malus law with terahertz metallic metamaterials for sensitive detection with giant tunable quality factor. *Phys. Rev. B* **2016**, *94*, 045407. [CrossRef]
34. Peng, Y.; Shi, C.J.; Xu, M.Q.; Kou, T.Y.; Wu, X.; Song, B.; Ma, H.Y.; Guo, S.W.; Liu, L.Z.; Zhu, Y.M. Qualitative and quantitative identification of components in mixture by terahertz spectroscopy. *IEEE Trans. Terahertz Sci. Technol.* **2018**, *8*, 696–701. [CrossRef]
35. Shanei, M.M.; Fathi, D.; Ghasemifard, F.; Quevedo-Teruel, O. All-silicon reconfigurable metasurfaces for multifunction and tunable performance at optical frequencies based on glide symmetry. *Sci. Rep.* **2019**, *9*, 13641. [CrossRef]
36. Liu, X.Y.; Li, F.Y.; Li, Y.X.; Tang, T.T.; Liao, Y.L.; Lu, Y.C.; Wen, Q.Y. Terahertz metasurfaces based on bound states in the continuum (BIC) for high-sensitivity refractive index sensing. *Optik* **2022**, *261*, 169248. [CrossRef]
37. Zhou, J.F.; Zhang, L.; Tuttle, G.; Koschny, T.; Soukoulis, C.M. Negative index materials using simple short wire pairs. *Phys. Rev. B* **2006**, *73*, 041101. [CrossRef]
38. Sohi, P.A.; Singh, P.; Kahrizi, M. Localized surface plasmon resonance biosensor designed for high refractive index volatile organic compound (VOC) biomarkers detection in visible spectrum. *Optik* **2022**, *257*, 168748. [CrossRef]
39. Zhao, J.; Zhang, L.; Liang, H.W. Advances in metasurface-based terahertz sensing. *Adv. Phys. Res.* **2024**, *3*, 2400077. [CrossRef]
40. Xue, Y.Y.; Li, J.S. Terahertz all-dielectric metasurface sensor based on quasi-bound states in the continuum. *Appl. Optics* **2023**, *62*, 1610–1615. [CrossRef]
41. Jadeja, R.; Surve, J.; Parmar, T.; Patel, S.K.; Al-Zahrani, F.A. Detection of peptides employing a THz metasurface based sensor. *Diam. Relat. Mat.* **2023**, *132*, 109675. [CrossRef]
42. Wang, G.Q.; Lang, T.T.; Hong, Z. Metallic metamaterial terahertz sensors for simultaneous measurement of temperature and refractive index. *Appl. Optics* **2020**, *59*, 5385–5390. [CrossRef]
43. Yang, J.H.; Lin, Y.S. Design of tunable terahertz metamaterial sensor with single- and dual-resonance characteristic. *Nanomaterials* **2021**, *11*, 2212. [CrossRef]
44. Zhang, J.H.; Zhang, S.J.; Dong, J.; Wang, M.; Luo, H.; Wu, R.G.; Xiao, C.W. Design of pixel terahertz metamaterial absorber sensor based on an improved ant colony algorithm. *IEEE Sens. J.* **2024**, *24*, 40801–40810. [CrossRef]
45. Niu, J.H.; Zhang, C.B.; Mo, W.; Weng, Z.J.; Cui, Y.F. Vanadium dioxide-based ultra-bandwidth/dual-narrowband switchable terahertz absorbers and sensing applications. *Appl. Optics* **2025**, *64*, 5679–5687. [CrossRef]

Disclaimer/Publisher's Note: The statements, opinions and data contained in all publications are solely those of the individual author(s) and contributor(s) and not of MDPI and/or the editor(s). MDPI and/or the editor(s) disclaim responsibility for any injury to people or property resulting from any ideas, methods, instructions or products referred to in the content.